2020-12

On the friction drag reduction mechanism of streamwise wall fluctuations

Jozsa, TI

http://hdl.handle.net/10026.1/17648

10.1016/j.ijheatfluidflow.2020.108686
International Journal of Heat and Fluid Flow
Elsevier BV

On the friction drag reduction mechanism of streamwise wall fluctuations

Tamás István Józsa[a,*], Elias Balaras[b], Maria Kashtalyan[c], Alistair George Liam Borthwick[d], Ignazio Maria Viola[e]

[a] *Department of Engineering Science, Institute of Biomedical Engineering, University of Oxford, Oxford OX1 3PJ, UK*
[b] *Department of Mechanical and Aerospace Engineering, The George Washington University, Washington, DC 20052, USA*
[c] *School of Engineering, Centre for Micro- and Nanomechanics (CEMINACS), University of Aberdeen, Aberdeen AB24 3UE, UK*
[d] *School of Engineering, Institute for Infrastructure and Environment, University of Edinburgh, Edinburgh EH9 3FB, UK*
[e] *School of Engineering, Institute for Energy Systems, University of Edinburgh, Edinburgh EH9 3FB, UK*

Abstract

Understanding how to decrease the friction drag exerted by a fluid on a solid surface is becoming increasingly important to address key societal challenges, such as decreasing the carbon footprint of transport. Well-established techniques are not yet available for friction drag reduction. Direct numerical simulation results obtained by Józsa *et al.* (2019) previously indicated that a passive compliant wall can decrease friction drag by sustaining the drag reduction mechanism of an active control strategy. The proposed compliant wall is driven by wall shear stress fluctuations and responds with streamwise wall velocity fluctuations. The present study aims to clarify the underlying physical mechanism enabling the drag reduction of these active and passive control techniques. Analysis of turbulence statistics and flow fields reveals that both compliant wall and active control amplify streamwise velocity streaks in the viscous sublayer. By doing so, these control methods counteract dominant spanwise vorticity fluctuations in the near-wall region. The lowered vorticity fluctuations lead to an overall weakening of vortical structures which then mitigates momentum transfer and

*Corresponding author
Email address: `tamas.jozsa@eng.ox.ac.uk` (Tamás István Józsa)

results in lower friction drag. These results might underpin the further development and practical implementation of these control strategies.

Keywords: Turbulent channel flow, Active flow control, Passive flow control, Drag reduction, Compliant wall, Compliant surface

2010 MSC: 76D55

1. Introduction

The question as to whether compliant walls can sustain drag reduction in turbulent flows has challenged fluid dynamicists in the decades [1] after Kramer's somewhat controversial experiments [2–4]. The early research focus was on quantification of the impact of deformable surfaces on transitional flows. Studies based on linear stability analysis of flat plate boundary layers demonstrated that a pressure-driven surface can delay laminar-turbulent transition by damping Tollmien-Schlichting waves [5, 6]. It was reported that a wall made of compliant panels could postpone natural transition indefinitely [7], and such transition delay was confirmed for in-plane channel flows [8]. Sixty years after Kramer's experiments, this phenomenon is now widely accepted owing to carefully conducted experiments [9–11] and numerical investigations [12, 13].

Later research studies have aimed to characterise the interaction of compliant surfaces and fully-developed turbulent flows. Theoretical [14] and experimental [15–17] studies suggested that travelling wave-like surface deformations could suppress turbulence production in turbulent boundary layers. Conversely, studies based on Direct Numerical Simulations (DNS) [18–22] and resolvent analysis [23, 24] reported minimal changes or increased friction drag in the presence of compliant surfaces. The results implied that pressure-driven wall-normal deformations cannot utilise the drag reduction mechanisms of opposition control [25–28] and streamwise-travelling waves [29] at low Reynolds numbers.

To date, experimental work has mostly targeted single-layer isotropic viscoelastic materials that exhibit primarily wall-normal deformations [9–11, 15–17, 30–32]. By comparison, the majority of computational studies solely examined pressure-driven compliant walls represented by dynamic systems with wall-normal displacement response [18, 20, 33]. Only a few studies have considered the effects of passive in-plane wall motions [19, 34–36]. Furthermore, computational studies on flow control have been restricted to low Reynolds numbers with few exceptions, such as [37].

Recently, it has been demonstrated by means of DNS that even small-scale spanwise deformations can act like a wall with spanwise slip [38] and result in substantial drag penalty [34]. The latter study also reported that a conceptual compliant wall can imitate streamwise active flow control originally proposed by [25]. Importantly, it was found that drag reduction is sustained by streamwise wall fluctuations driven by streamwise wall shear stress fluctuations.

The present study aims to examine the drag reduction mechanism of active and passive flow control techniques with streamwise wall velocity responses at low and moderate Reynolds numbers for the first time. To this end, a database of controlled and uncontrolled canonical turbulent channel flows at low and moderate friction Reynolds numbers ($Re_\tau \approx 180$ and 1000) is analysed and extended with flow visualisations, Reynolds stress transport statistics and Lagrangian wall motion tracking [39]. The paper is structured as follows. Section 2 outlines the computational methodology. Section 3 presents the main results for active and passive control methods in terms of integral variables, the fluctuating flow field, turbulence statistics, and Lagrangian wall motions. Section 4 lists the main findings. It should be noted that preliminary results were presented at the Eleventh International Symposium on Turbulence and Shear Flow Phenomena (TSFP11) [40].

2. Methods

2.1. Simulation Settings

Herein, fully-developed turbulent flow in an idealised plane channel is modelled by the incompressible continuity and Navier-Stokes momentum equations (see e.g. [41]), which are discretised on a Cartesian staggered grid and solved

Table 1: Simulation settings. L_1, L_2, and L_3 are the streamwise, wall-normal and spanwise lengths of the computational domain, and n_1, n_2, and n_3 are the corresponding grid resolutions. Δt denotes the time step, whereas t_a is the averaging time.

Case	low Re	moderate Re
Reynolds number, Re	2857	20000
friction Reynolds number, Re_τ	180.7 ($\approx$ 180)	990.2 ($\approx$ 1000)
domain size, $L_1 \times L_2 \times L_3$	$4\pi \times 2 \times 4\pi/3$	$2\pi \times 2 \times \pi$
number of nodes, $n_1 \times n_2 \times n_3$	$290 \times 251 \times 290$	$770 \times 1001 \times 770$
temporal resolution, $\Delta t u_\tau^2/\nu$	≈ 0.115	≈ 0.196
averaging time, $t_a u_\tau^2/\nu$	≈ 23000	≈ 19600

numerically by an in-house fractional step solver [42]. Spatial derivatives are represented by second-order central-differences. The pressure-Poisson equation is solved directly [43] using fast Fourier transforms in the periodic (streamwise and spanwise) directions, and by a standard tridiagonal matrix algorithm [44] in the wall-normal direction. For time integration, an explicit third-order low-storage Runge-Kutta method is utilised for the streamwise and spanwise momentum equations, whereas the implicit Crank-Nicolson scheme is used for the wall-normal momentum equation. A detailed description of the in-house incompressible Navier-Stokes solver is given by [45].

We denote the streamwise, wall-normal, and spanwise Cartesian coordinates in the channel as x_1, x_2, x_3, and the corresponding velocity and vorticity components as u_1, u_2, u_3, and ω_1, ω_2, ω_3. Non-dimensional quantities are based on the channel half-height δ and bulk velocity u_b. The (bulk velocity) Reynolds number is defined as $Re = u_b\delta/\nu$, where ν denotes kinematic viscosity. Quantities with + superscripts are non-dimensionalised with respect to the friction velocity $u_\tau = \sqrt{\langle\tau_1\rangle/\rho}$ and the viscous length scale $\delta_\nu = \nu/u_\tau$ of the baseline (uncontrolled) simulations. The friction Reynolds number is defined as $\mathrm{Re}_\tau = u_\tau\delta/\nu$. Here, ρ is the fluid density and τ_1 is the streamwise wall shear stress component. The angled brackets $\langle\ \rangle$ indicate an averaged variable and the prime symbol $'$ denotes a fluctuating quantity. Table 1 lists the basic simulation settings. For further details of the model and its verification and validation tests, the reader is referred to [34, 39].

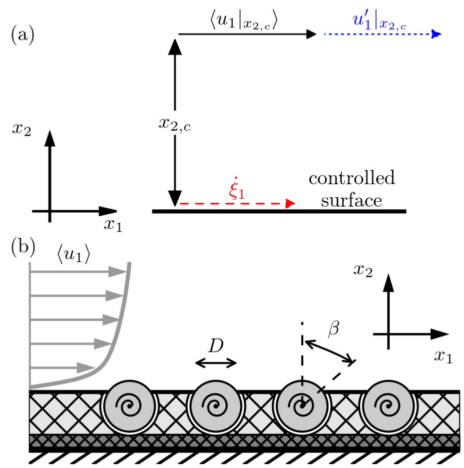

Figure 1: Schematic drawing of the implemented flow control techniques introducing streamwise wall fluctuations: (a) active control based on Eq. (1); (b) a compliant wall model including mounted rotating discs with spanwise aligned axes. The compliant wall is modelled using Eq. (2). These figures are modified with permission from Józsa *et al.* [34].

2.2. Boundary Conditions

The streamwise (x_1) and spanwise (x_3) directions are by definition periodic. In the uncontrolled (baseline) simulations, the channel walls (bounding x_1-x_3 planes) are hydrodynamically smooth no-slip walls. The active flow control and the compliant wall impose two different Dirichlet boundary conditions for the streamwise wall velocity component at both channel walls. The other two velocity components and the wall-normal pressure gradient at the channel walls are set to zero. Figure 1(a) shows the active flow control introduced in [25], where the fluctuating streamwise fluid velocity is measured at $x_{2,c}$ distance from the wall ($u_1'|_{x_{2,c}}$, sensing), and the wall velocity directly below the measurement location is equal to the measured streamwise velocity fluctuation both in direction and magnitude ($\dot{\xi}_1 = u_1|_{\text{wall}}$, actuation). Based on figure 1(a), the active flow control is implemented as

$$\dot{\xi}_1 = u_1'|_{x_{2,c}} = u_1|_{x_{2,c}} - \langle u_1|_{x_{2,c}} \rangle. \tag{1}$$

The compliant wall case exploits a drag reduction mechanism similar to that of active flow control, with streamwise wall shear stress component (τ_1) as input and streamwise wall velocity components ($u_{1,\mathrm{wall}}$) as output [34, 39, 40]. Figure 1(b) shows a conceptual model of such a compliant surface utilising mounted discs, inspired by a former active control study [46]. These discs have finite spanwise extent that is comparable to the viscous length scale (δ_ν). Therefore, the wall velocity response of the compliant surface exhibits streamwise and spanwise variations which are required for a successful control, as demonstrated in Sections 3.2 and 3.4. With sufficiently small disc diameter (D) and β angle (e.g. $D \sim \delta_\nu$ and $\beta < \pi/6$), a simplified dimensionless governing equation of the compliant wall can be written as

$$\underbrace{\frac{4C_m}{D^2 A_s}}_{\Lambda_m}\ddot{\xi}_1 + \underbrace{\frac{4C_d}{D^2 A_s}}_{\Lambda_d}\dot{\xi}_1 + \underbrace{\frac{4C_s}{D^2 A_s}}_{\Lambda_s}\xi_1 = \frac{1}{Re}\frac{\partial u_1}{\partial x_2}\bigg|_{\mathrm{wall}}, \tag{2}$$

assuming that the motion of the discs is driven by the local wall shear stress. Here, Λ_m, Λ_d and Λ_s are the inertia, damping, and spring stiffness parameters of the compliant surfaces, respectively. These parameters are proportional to the moment of inertia (C_m), viscous damping (C_d), and torsion spring coefficient (C_s) of a single mounted disc, and inversely proportional to its wetted surface area (A_s). In Eq. (2), ξ_1 is the tangential displacement of a disc. The resulting tangential velocity is assumed to be equivalent to the introduced streamwise wall velocity ($\dot{\xi}_1 = u_{1,\mathrm{wall}}$). If the β angle shown in Fiure 1(b) is less than $30°$, then this approximation leads to less than 5% error in the streamwise wall velocity compared to the exact formulation which accounts for the Cartesian velocity distribution over the disc surface [39]. Considering that the surface integral of the wall-normal velocities over the wetted surface is zero, the disc diameter is restricted so that the impact of the introduced wall-normal velocity is negligible.

During compliant wall simulations, Eq. (2) is imposed at every wall cell. To advance Eq. (2) in time, a fourth order Runge-Kutta scheme is employed, and a weak coupling scheme is implemented to treat the resulting fluid-structure interaction problem. The governing equation of the compliant surface ensures that the average streamwise wall velocity remains zero ($\langle u_1 \rangle = 0$) because the average displacement of the discs balances the average streamwise wall shear stress.

2.3. Measuring Control Effects

To keep the volumetric flow rate constant, the driving pressure gradient ($\partial P/\partial x_1$) is adjusted at every time step. With this in mind, the Drag Reduction (DR) in the case of controlled simulations is defined as

$$\mathrm{DR} = 1 - \frac{\langle \partial P/\partial x_1 \rangle_{\text{controlled}}}{\langle \partial P/\partial x_1 \rangle_{\text{baseline}}}. \tag{3}$$

In addition, the following global (integral) variables are introduced to quantify the effects of the control methods on the entire flow field [47]. Using the Einstein summation convention, the global turbulent kinetic energy is defined as

$$k_g = \frac{1}{\delta}\int_0^{\delta} k \mathrm{d}x_2 = \frac{1}{\delta}\int_0^{\delta} \frac{\langle u_i' u_i' \rangle}{2} \mathrm{d}x_2. \tag{4}$$

Similarly, the global turbulent enstrophy is computed from the fluctuating vorticity components as

$$\mathcal{E}_g = \frac{1}{\delta}\int_0^{\delta} \mathcal{E} \mathrm{d}x_2 = \frac{1}{\delta}\int_0^{\delta} \langle \omega_i' \omega_i' \rangle \, \mathrm{d}x_2. \tag{5}$$

Furthermore, the absolute change (Δ) and the relative change (Δ_r) of a general quantity (q) are defined as

$$\Delta q = q_{\text{controlled}} - q_{\text{baseline}}, \tag{6}$$

and

$$\Delta_r q = \frac{q_{\text{controlled}} - q_{\text{baseline}}}{q_{\text{baseline}}}. \tag{7}$$

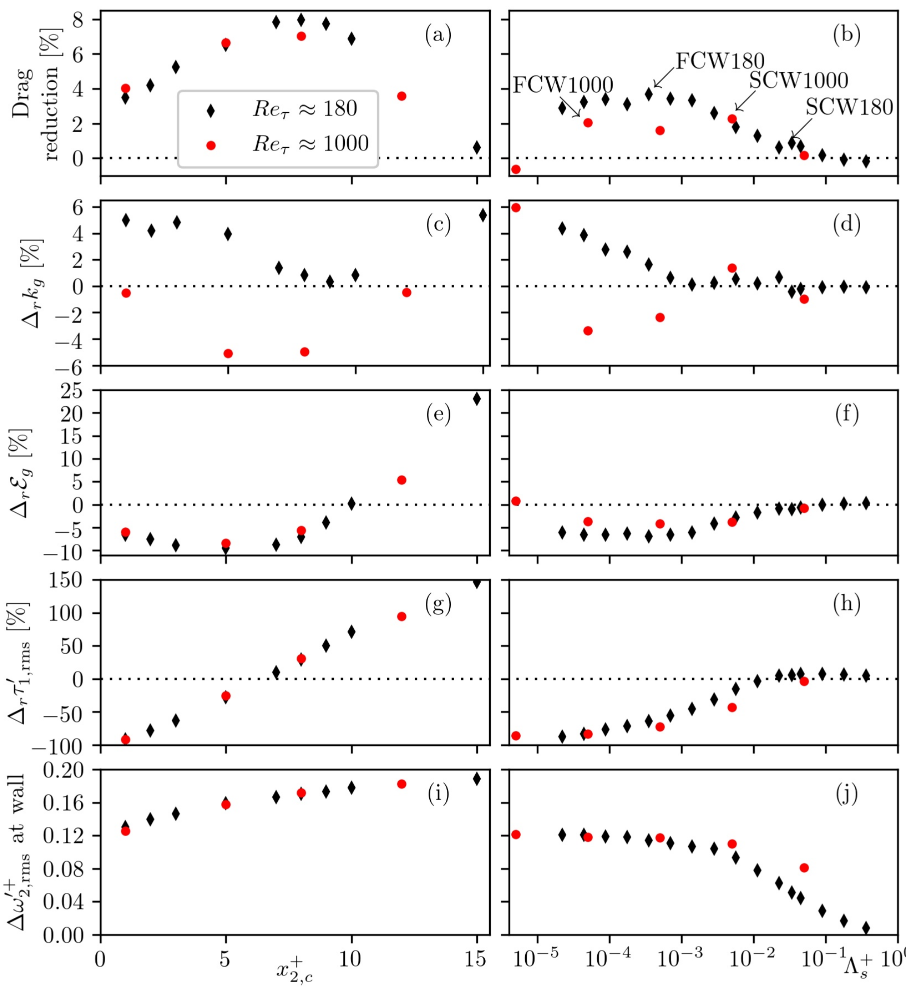

Figure 2: Effects of the active and passive control techniques on drag reduction (a)-(b), relative change in global turbulent kinetic energy (c)-(d), relative change in global turbulent enstrophy (e)-(f), relative change in rms streamwise wall shear stress fluctuations (g)-(h), and absolute change in rms wall-normal vorticity fluctuations at the wall (i)-(j), as functions of control distance (left column) and spring parameter (right column), respectively. The dotted lines indicate the zero level.

3. Results and Discussion

3.1. Integral variables

Figure 2 shows the effect of different control cases on certain integral variables listed in Section 2.3. From Figures 2(a) and (g), it can be seen that the Active Flow Control (AFC) with $x^+_{2,c} = 1$ leads to ca. 4% drag reduction accompanied with a more than 90% drop in the root-mean-square (rms) streamwise wall shear stress fluctuations $\tau'_{1,\mathrm{rms}}$ at $Re_\tau \approx 180$ and 1000. Maximum drag reductions of 8% and 7% at $Re_\tau \approx 180$ and 1000 respectively are attained for active control with $x^+_{2,c} = 8$. Active control also performs well when the global turbulent enstrophy is decreased, as indicated in Figure 2(e). However, it is somewhat counter-intuitive that (i) maximum drag reduction occurs when there is a 30% increase in $\tau'_{1,\mathrm{rms}}$; and (ii) drag reduction is accompanied by an increase in global turbulent kinetic energy at $Re_\tau \approx 180$. This behaviour can be observed in Figures 2(a), (c), and (g). From Figure 2(g), it can be concluded that active control can have fluctuating shear-cancelling and shear-increasing modes corresponding to decreased ($\Delta_r \tau'_{1,\mathrm{rms}} < 0$) and increased ($\Delta_r \tau'_{1,\mathrm{rms}} > 0$) streamwise wall shear stress fluctuations, respectively. Both modes are tied to an increase in wall-normal vorticity fluctuations as shown in Figure 2(i). Sections 3.2 and 3.3 aim to explain these observations based on analyses of the flow fields and turbulence statistics, respectively.

The three-dimensional parameter space of the compliant wall is mapped using a semi-analytical method, following [34, 35]. Using the resulting framework, we optimise parameters for maximal $\tau'_{1,\mathrm{rms}}$, noting that active control provides maximum drag reduction when in a shear-increasing mode [39]. DNS at $Re_\tau \approx 180$ reveals that the resulting parameter set corresponds to a Stiff Compliant Wall (SCW180), increases $\tau'_{1,\mathrm{rms}}$ by ca. 6%, and has a marginal impact on friction drag (see Table 2). Taking SCW180 as the starting point, a parameter sweep is performed by changing solely the spring parameter for simplicity, as shown in Figure 2. The results presented in Figure 2(h) confirm that compliant walls sustaining streamwise velocity fluctuations have shear-cancelling ($\Delta_r \tau'_{1,\mathrm{rms}} < 0$) and shear-increasing ($\Delta_r \tau'_{1,\mathrm{rms}} > 0$) modes, similar to active control. Figure 2(b) shows a Flexible Compliant Wall (FCW180) corresponding to peak drag reduction measured in the present study (see Table 2). FCW180 results in 3.68% drag reduction at $Re_\tau \approx 180$ which is more than twice the maximum value reported by other computational studies on compliant surfaces (1.7%) [20]. Considering other passive control techniques, the peak drag reduction is lower than the value measured with riblets (≈8%) [48–50] but higher than the value measured with wavy walls (0.6%) [51]. FCW180 has been tested for modified domain sizes, spatial and temporal resolutions, and sample sizes, and a thorough error quantification found a ±1% uncertainty in drag reduction [34]. The domain size has been identified as the primary error source. Therefore ±1% drag reduction uncertainty is representative of the low Reynolds number cases but simulations at $Re_\tau \approx 1000$ suffer from a somewhat larger uncertainty. Detailed uncertainty quantification for the $Re_\tau \approx 1000$ case is an outstanding challenge because simulations at moderate Reynolds numbers, especially with increased domain size, are extremely resource intensive

Table 2: Parameters of selected compliant walls (SCW180, FCW180, etc.) and corresponding drag reduction (DR).

ID	$Re_\tau \approx$	Λ_m	Λ_d	Λ_s	DR [%]
SCW180	180	$1.40 \cdot 10^{-3}$	0	$3.38 \cdot 10^{-2}$	0.86
FCW180	180	$1.40 \cdot 10^{-3}$	0	$3.50 \cdot 10^{-4}$	3.68 ± 1
SCW1000	1000	$4.00 \cdot 10^{-4}$	0	$5.00 \cdot 10^{-3}$	2.29
FCW1000	1000	$4.00 \cdot 10^{-4}$	0	$5.00 \cdot 10^{-5}$	2.04

Simulations are carried out at $Re_\tau \approx 1000$ to gain insight into the effect of increasing Reynolds number (Table 2 and Figure 2). The inertia parameter, Λ_m is decreased for these simulations to ensure that compliant surfaces remain responsive. The investigated parameters lead to significant performance degradation with increasing Reynolds number but both FCW180 and FCW1000 sustain a considerable decrease in $\tau'_{1,\mathrm{rms}}$ accompanied with drag reduction. According to Figure 2(b), the drag reduction curve breaks down with decreasing spring parameter. Hence, $\tau'_{1,\mathrm{rms}} = 0$ is not optimal for passive control. We find that stiffer compliant walls can perform better at $Re_\tau \approx 1000$ compared to $Re_\tau \approx 180$ (see SCW180 and SCW1000 in Table 2 and Figure 2(b)). Although, the impacts of the other parameters (Λ_m and Λ_d) at $Re_\tau \approx 180$ have been reported in our previous studies [34, 39], the parameter space at $Re_\tau \approx 1000$ remains mostly unexplored because of the associated high computational cost.

Pairwise comparisons between Figures 2 (g)-(h) and (i)-(j) suggest that as $\Lambda_s \to 0$, the effect of passive control on wall quantities approaches that of active control with $x^+_{2,c} = 1$. The source of this similarity is determined through manipulation of the control equations. Substituting a Taylor series expansion of u'_1 near the wall into Equation (1) leads to

$$\left.\frac{\partial u'_1}{\partial x_2}\right|_{\text{wall}} x_{2,c} + \frac{1}{2}\left.\frac{\partial^2 u'_1}{\partial x_2^2}\right|_{\text{wall}} x^2_{2,c} + \mathcal{O}(x^3_{2,c}) = 0. \tag{8}$$

This equation suggests that if the control distance is small ($x^+_{2,c} = 1$) then the active control cancels the spanwise vorticity fluctuations at the wall:

$$\omega'_{3,\text{wall}} = -\left.\frac{\partial u'_1}{\partial x_2}\right|_{\text{wall}} = -\frac{\tau'_1}{\rho\nu} = 0. \tag{9}$$

With respect to passive control, Equation (2) tends to Equation (9) as the control parameters tend to zero ($\Lambda_m \to 0$, $\Lambda_d \to 0$, and $\Lambda_s \to 0$, leading to $\tau'_1 \to 0$). This prediction regarding the asymptotic behaviour of the passive control overlaps with the result of parameter space mapping reported in [34, 39].

3.2. Fluctuating Flow Field Analysis

Both the active and passive control methods interact primarily with the so called near-wall cycle that comprises quasi-streamwise vortices and streamwise velocity streaks driven by the mean shear [52]. Figure 3 illustrates the three-dimensional arrangement of typical instantaneous vortical features, including a hairpin vortex formation [53] and the connected counter-rotating vortices [52, 54]. The streamwise control techniques do not noticeably modify these vortical features [39]. Visualisation of the vorticity field offers an alternative method by which to detect qualitative changes in the flow field, and has been proven to be an efficient means to understand flow control [55]. Here, the vorticity field is explored by seeding vorticity lines of the instantaneous fluctuating flow field as visualised in Figure 3. In Figure 3, the high and low momentum regions (streaks) corresponding to the vortical features are represented by the fluctuating vorticity lines. Within the streaks, where streamwise fluctuations and the corresponding shear dominate, fluctuating vorticity lines ($\boldsymbol{\omega}'$ lines) form a spiral shape with quasi-streamwise aligned axis.

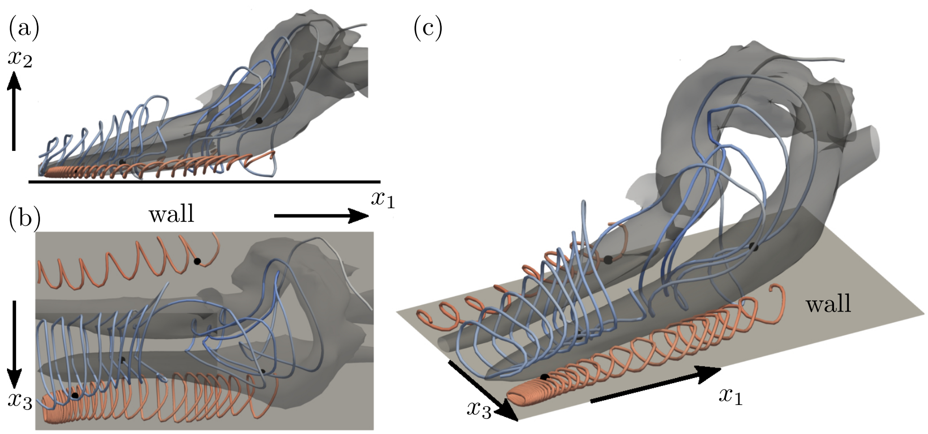

Figure 3: Instantaneous flow features near the wall at $\mathrm{Re}_\tau \approx 1000$: (a) side view; (b) top view; (c) bird's eye view. The total wall-normal extent of the $Q = 35$ isosurface [56] is about $100\delta_\nu$. The streamwise and spanwise extent of the presented wall section is $190\delta_\nu$, and $110\delta_\nu$, respectively. The black spheres indicate fluctuating vorticity line seeding points. A hairpin vortex is formed around the blue fluctuating vorticity lines enclosed by a low momentum region. The remaining two red vorticity lines are enclosed by high momentum regions.

We now summarise the key kinematic properties of fluctuating vorticity lines with increasing wall distance based on Figure 3 and baseline velocity and vorticity statistics given in Appendix A. First, $\omega_3' \gg \omega_1' > \omega_2'$, and hence $\boldsymbol{\omega}'$ lines lie parallel to the x_1-x_3 plane. Near the wall, $\omega_3' \approx -\partial u_1'/\partial x_2 \propto \tau_1'$ represents flow shear between the streaks and the wall. Fluctuating vorticity lines are directed towards the wall-normal direction between the low- and high-momentum streaks, highlighting that $\omega_2' \approx -\partial u_1'/\partial x_3$. In the buffer layer, streak instabilities emerge [52] as the viscous force weakens. The streamwise vorticity (ω_1') exhibits a statistical local maximum at about $x_2^+ = 20$, corresponding to the mean wall distance of the centre-line of quasi-streamwise vortices. If $x_2^+ \ll 20$, then $\omega_1' \approx \partial u_3'/\partial x_2 \propto \tau_3'$ gives a measure of shear between the wall and quasi-streamwise vortices. For $x_2^+ > 50$, vorticity fluctuations, unlike velocity fluctuations, are approximately isotropic [54], i.e. $\langle \omega_1'\omega_1' \rangle \approx \langle \omega_2'\omega_2' \rangle \approx \langle \omega_3'\omega_3' \rangle$. Above $x_2^+ \approx 100$, hairpin vortices can be detected by the Q-criterion or vorticity line bundles but vorticity lines are mostly disorganised [57, 58]. At the Reynolds numbers investigated in this study, fluctuating vorticity lines remain rooted in the viscous sublayer suggesting that the entire flow field is attached to the wall and can be modified by wall motions.

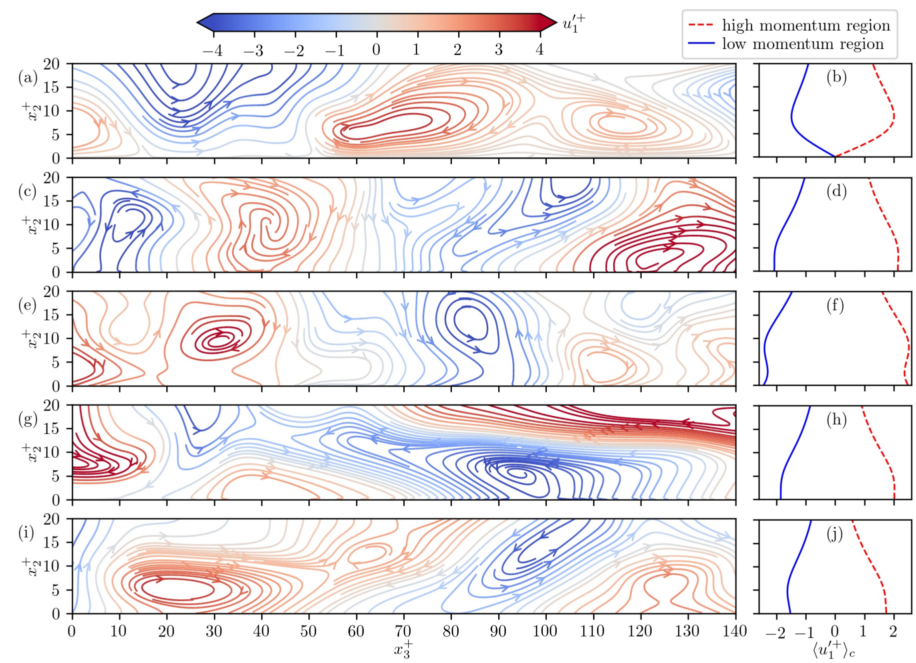

Figure 4: Effects of active and passive control techniques on instantaneous near-wall $\boldsymbol{\omega}'$ lines (left column) and $\langle u_1' \rangle_c$ profiles (right column) at $\mathrm{Re}_\tau \approx 1000$. The $\boldsymbol{\omega}'$ lines are visualised along a cross-section and are coloured by u_1'. Baseline case (a)-(b), active control with $x_{2,c}^+ = 1$ (c)-(d), active control with $x_{2,c}^+ = 8$ (e)-(f), FCW1000 (g)-(h), SCW1000 (i)-(j). Similar trends can be observed at $\mathrm{Re}_\tau \approx 180$.

Next, these vorticity features are investigated in the controlled channels, as depicted in the left column of Figure 4. In addition, conditionally averaged streamwise velocity profiles ($\langle u_1' \rangle_c$) of the low and high momentum regions are presented in the right column of Figure 4. These regions are distinguished according to the sign of the streamwise wall shear stress fluctuations and the sign of the wall velocity fluctuations in the baseline and controlled cases, respectively. The left column of Figure 4 suggests that the walls become part of the streamwise velocity streaks as a result of the control. The $\boldsymbol{\omega}'$ lines highlight a twofold impact on the near-wall vorticity fluctuations: (i) spanwise vorticity fluctuations are suppressed; and (ii) wall-normal vorticity fluctuations are introduced. The flattened velocity profiles in the right column of Figure 4 confirm spanwise vorticity cancellation in the case of actively and passively controlled walls. The streaky wall motions promoted by the control methods induce wall-normal vorticity at the wall, as shown in Figures 2(i)-(j). The increased wall-normal vorticity component ω_2 relates to enhanced shear-layers between low- and high-momentum streaks (see Figure 4(c), (e), (g), and (i)).

In shear-increasing mode, active control amplifies ω_3' very close to the wall because of reversed shear, as depicted in Figure 4(f). This behaviour can be deduced from the second order approximation of the active control equation:

$$\left.\frac{\partial u_1'}{\partial x_2}\right|_{\text{wall}} > 0 \text{ if } \left.\frac{\partial^2 u_1'}{\partial x_2^2}\right|_{\text{wall}} < 0, \tag{10}$$

and *vice versa*. Therefore, active control naturally creates a velocity profile with reversed shear as $x_{2,c}$ increases. Active control attains peak performance by reversing fluctuating shear at the wall, and thus cancelling the dominant spanwise vorticity fluctuations. Sustaining such states requires energy input and hence it is not possible with a passive compliant surface [34].

It appears that a decrease in net vorticity fluctuations at the wall damps vorticity fluctuations throughout the boundary layer, and mitigates momentum transfer which in turn contributes to turbulent friction drag. Wall motions induced by the control techniques lower spanwise vorticity fluctuations by decreasing the shear between wall and streaks; this process inevitably increases shear between the streaks. Amplified shear between the streaks manifests itself as increased wall-normal vorticity in the near-wall region (shown in Figures 2(i) and (j)), which is undesirable according to the above hypothesis. Consequently, streamwise control has simultaneously positive and negative effects which limit the control performance and cause the corresponding drag reduction curve to break down.

In summary, streamwise wall motions dictated by the control methods can reduce spanwise vorticity fluctuations (i.e. shear between the streaks and wall) but increasingly build up undesirable wall-normal vorticity fluctuations (i.e shear between the streaks) by doing so. For this reason, streamwise wall fluctuations can weaken turbulence when ω_3' cancellation dominates over ω_2' amplification but such wall motions cannot relaminarise the flow. In this sense, this drag reduction mechanism is unique. By comparison, wall-normal and spanwise opposition control [25–28] and spanwise wall oscillations [37, 59, 60] increase near-wall vorticity fluctuations to counteract quasi-streamwise vortices and weaken the near-wall cycle (which is known to be a major contributor to turbulence production).

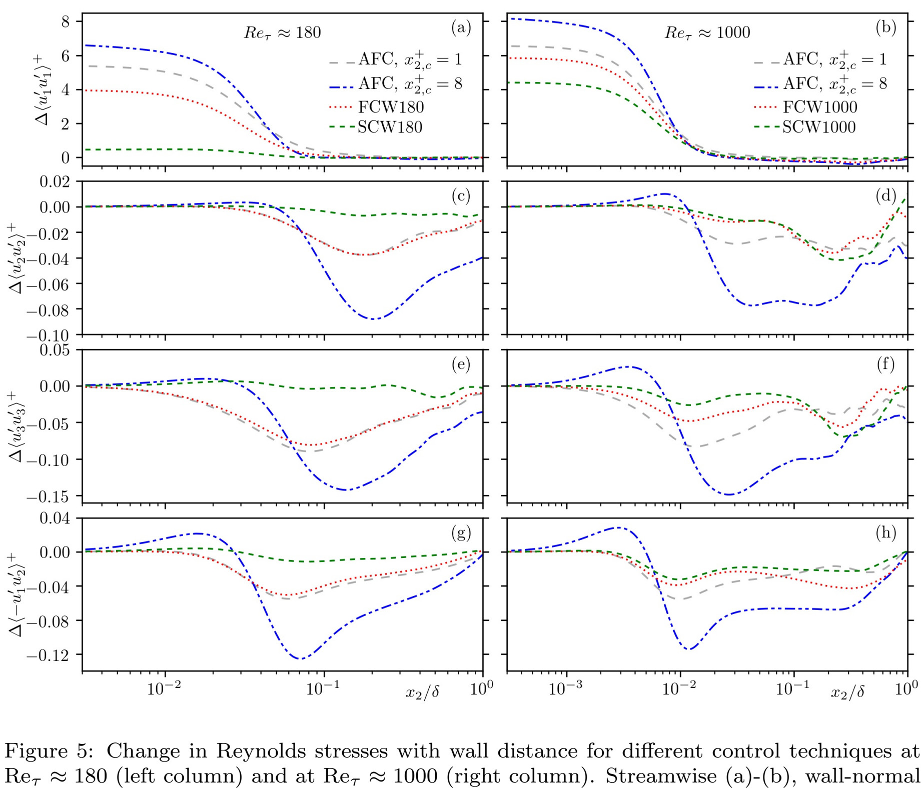

Figure 5: Change in Reynolds stresses with wall distance for different control techniques at $\mathrm{Re}_\tau \approx 180$ (left column) and at $\mathrm{Re}_\tau \approx 1000$ (right column). Streamwise (a)-(b), wall-normal (c)-(d), spanwise (e)-(f) components, and Reynolds shear stress (g)-(h).

3.3. Turbulence Statistics

To investigate the drag reduction mechanism, we examine how the control methods modify turbulence statistics in comparison to baseline values available in Appendix A. The control techniques cause qualitative changes only in the most energetic streamwise velocity fluctuations characterised by $\langle u_1' u_1' \rangle$. Figures 5(a) and (b) indicate that the control methods amplify streamwise velocity streaks by inducing significant streamwise fluctuations in the near-wall region. In exchange, a slight drop in the remaining Reynolds stress components is evident from Figures 5(c)-(h). According to Figure 5(a), the global turbulent kinetic energy at $Re_\tau \approx 180$ is increased (Figure 2(c)-(d)) when the control methods are applied because the amplified streaks fill about 10% of the channel. At $Re_\tau \approx 1000$, the control techniques energise the streaks similarly, but with increasing Reynolds number the wall-normal extent of the streaks reduces. Based on Figure 5(b), near-wall streaks occupy only ca. 2% of the channel at $Re_\tau \approx 1000$. In addition, at $Re_\tau \approx 1000$, the control methods weaken the large-scale motions of the log-layer, which contain most of the turbulent kinetic energy at high Reynolds numbers [61, 62]. This phenomenon can be observed in Figure 5(b), where $\Delta\langle u_1' u_1' \rangle$ is negative above $x/\delta = 0.05$. The increase in $\langle u_1' u_1' \rangle$ in Figure 5(a)-(b), and decreases in $\langle u_2' u_2' \rangle$, $\langle u_3' u_3' \rangle$, and $\langle -u_1' u_2' \rangle$ visible in Figure 5(c)-(h) suggest that momentum transfer decreases between the streamwise and other velocity components compared to the baseline case.

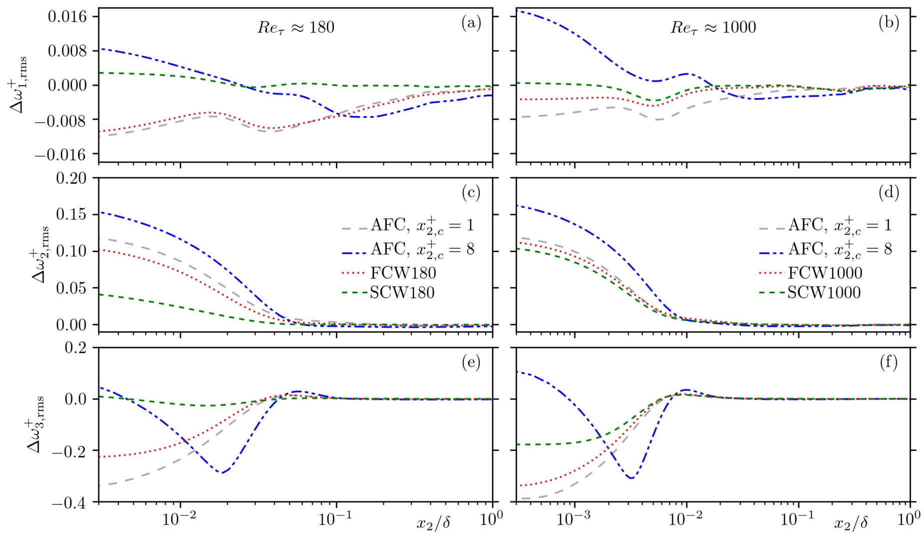

Figure 6: Change in root-mean-square fluctuating vorticity components with wall distance for different control techniques at $\mathrm{Re}_\tau \approx 180$ (left column) and at $\mathrm{Re}_\tau \approx 1000$ (right column). Streamwise (a)-(b), wall-normal (c)-(d), and spanwise (e)-(f) components.

The streamwise wall motions of the control methods directly modify the spanwise vorticity fluctuations depicted in Figure 4. Figure 6(e)-(f) shows unequivocally the strong influence of the control techniques on the spanwise vorticity fluctuations (and therefore on streamwise wall shear stress fluctuations), especially in the near-wall region. The rms spanwise vorticity profiles underline that the active control in shear-cancelling mode ($x^+_{2,c} = 1$) and efficient compliant walls, such as FCW180, FCW1000, and SCW1000, damp spanwise vorticity fluctuations at the wall. In shear-increasing mode, the active control amplifies ω'_3 very close to the wall. However, as depicted by the lines corresponding to $x^+_{2,c} = 8$ in Figures 6(e) and (f), the increase in ω'_3 at the wall turns into a net cancellation of ω'_3 in the near-wall region. This behavour is a direct consequence of the fluctuating velocity profiles with reversed shear, as visualised in Figure 4(f).

The rms wall-normal vorticity profiles (ω'_2) in Figures 6(c)-(d) confirm that the control methods introduce statistically significant wall-normal vorticity fluctuations representing increased shear between the streaks. Whereas FCW180, FCW1000 and the active control with $x_{2,c}^+ = 1$ lower ω_1' throughout the domain, streamwise vorticity fluctuations are amplified in the vicinity of the wall in the case of active control with $x_{2,c}^+ = 8$ and SCW180 and SCW1000 according to Figures 6(a)-(b). In every case where statistically significant drag reduction (more than 1%) occurs, vorticity fluctuations are increased only in the near-wall regions, which account for 10% and 2% of the channels, at $\mathrm{Re}_\tau \approx 180$ and 1000, respectively. Figures 6(a)-(d) and Figures 6(e)-(f) reveal that successful control methods weaken vorticity fluctuations throughout the majority of the channel compared to the baseline case, owing to spanwise vorticity cancellation near the wall.

The near-wall cycle contributes significantly to turbulence production in boundary layers [52]. Nonlinear interactions between the mean flow, quasi-streamwise vortices, and velocity streaks redistribute near-wall streamwise momentum fluctuations first to spanwise and then to wall-normal momentum fluctuations as the wall distance increases [54]. The negative regime of the $\Delta_r \omega'_{1,\mathrm{rms}}$ curves in Figures 6(a)-(b) implies that quasi-streamwise vortices are weakened by the control. For this reason, a lower turbulence production and inter-component momentum transfer compared to the baseline case should be measurable based on the Reynolds stress budgets.

The Reynolds stress transport equation [41, 63] for statistically steady state turbulent flows reads as

$$\langle u_k \rangle \frac{\partial \left\langle u_i' u_j' \right\rangle}{\partial x_k} = P_{ij} + T_{ij} + \Pi_{ij} + D_{ij} + \epsilon_{ij}. \tag{11}$$

where P_{ij} is the production rate, T_{ij} is the turbulent transport rate, Π_{ij} denotes the velocity-pressure gradient term, D_{ij} is the viscous diffusion rate, and ϵ_{ij} is the dissipation rate of the corresponding Reynolds stress components. Expanding these terms from the right hand side of Eq. (11) leads to

$$
\begin{aligned}
P_{ij} &= -\left\langle u_i' u_k' \right\rangle \frac{\partial \left\langle u_j \right\rangle}{\partial x_k} - \left\langle u_j' u_k' \right\rangle \frac{\partial \left\langle u_i \right\rangle}{\partial x_k}; \\
T_{ij} &= -\frac{\partial \left\langle u_i' u_j' u_k' \right\rangle}{\partial x_k}; \\
\Pi_{ij} &= -\left\langle u_i' \frac{\partial p'}{\partial x_j} \right\rangle - \left\langle u_j' \frac{\partial p'}{\partial x_i} \right\rangle; \\
D_{ij} &= \frac{1}{\mathrm{Re}} \frac{\partial^2 \left\langle u_i' u_j' \right\rangle}{\partial x_k \partial x_k} \text{ and} \\
\epsilon_{ij} &= -\frac{2}{\mathrm{Re}} \left\langle \frac{\partial u_i'}{\partial x_k} \frac{\partial u_j'}{\partial x_k} \right\rangle.
\end{aligned} \tag{12}
$$

Thereafter, turbulent kinetic energy transport terms can be computed based on Equations (4) and (11) so that, for instance, $P_k = P_{ii}/2$.

Baseline turbulent kinetic energy and Reynolds shear stress budgets are listed in Appendix B. Regarding near-wall turbulent kinetic energy transport, the control techniques cause the most distinct increase in dissipation (less loss) balanced by diffusion (D) as shown in Figures 7(a) and (b). Global turbulent kinetic energy dissipation is linked to global enstrophy [47], and hence the control techniques weaken dissipation (the leading loss term of turbulent kinetic energy) by reducing vorticity fluctuations. Weakened turbulent dissipation is naturally accompanied by amplified near-wall (mainly streamwise) fluctuations.

The sum of the velocity-pressure gradient term and the turbulent transport rate ($\Pi_{ij} + T_{ij}$) dictates momentum distribution between the diagonal Reynolds stress components [63]. From Figures 7(a) and (b), decreased $\Pi + T$ is evident highlighting that the control techniques indeed mitigate inter-component momentum transport. Therefore, in the successful controlled cases, fluctuations remain somewhat restricted to the streamwise velocity component. The corresponding suppressed momentum transfer between the mean flow and the fluctuations is symbolised by turbulent kinetic energy and Reynolds shear stress production decay as shown in Figures 7(a)-(d). According to the Fukagata-Iwamoto-Kasagi identity [64], suppressing the integrated Reynolds shear stress is equivalent to drag reduction. The statistical analysis of the control techniques emphasises a connection between vorticity fluctuations and drag reduction which overlaps with the findings of previous studies uncovering links between friction drag, enstrophy [47] and velocity-vorticity correlations [65].

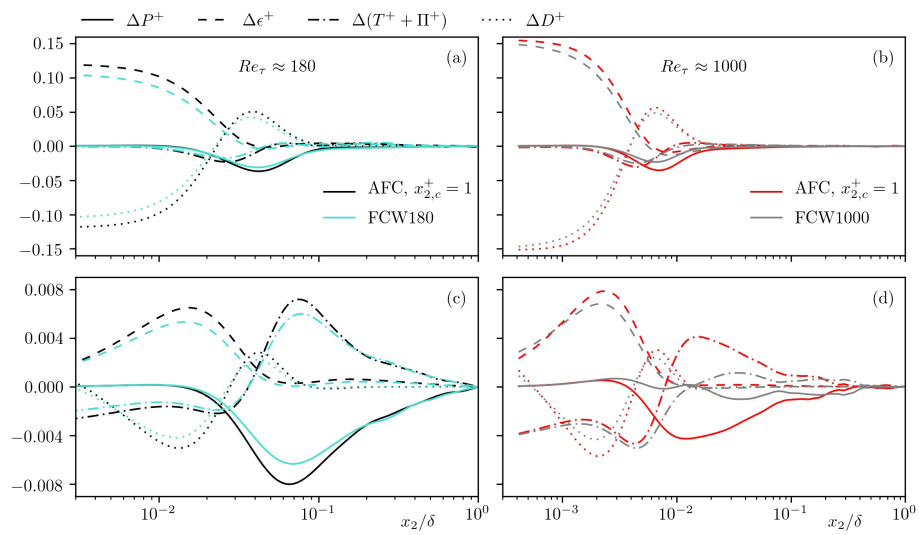

Figure 7: Change in turbulent kinetic energy and Reynolds shear stress transport terms with wall distance for different control techniques at $\mathrm{Re}_\tau \approx 180$ (left column) and $\mathrm{Re}_\tau \approx 1000$ (right column). Turbulent kinetic energy (a)-(b), and Reynolds shear stresses $-\langle u_1' u_2' \rangle$ (c)-(d).

3.4. Lagrangian Wall Motions

Finally, wall motions of the compliant surfaces are analysed to evaluate their realisation potential. To this end, the solely streamwise Lagrangian displacement field of the wall is determined by integrating the velocity field. Considering the mounted rotating disc model in Figure 1(b), the analysed Lagrangian displacement field describes points travelling from one disc to another. For video sequences visualising the wall velocity and the displacement fields, see the Supplementary Data available online.

The material lines corresponding to SCW180 preserve their consistency and exhibit standing wave-like movements but such wall motions are not sufficient to sustain statistically significant friction drag reduction (see Table 2). By comparison, in the case of FCW180, the wall needs to support large deformations in positive and negative directions within a short distance in order to cancel wall shear stress fluctuations originating from streaks. After the material points are clustered in the neighbourhood of low wall velocity regions between streaks, they travel together. Both FCW1000 and SCW1000 behave similarly to FCW180 resulting in dense and sparse wall sections which are difficult to realise beyond the conceptual rotating disc model. Representative rms displacement values for the selected compliant walls are summarised in Table 3.

Table 3: Root-mean-square displacement values corresponding to selected compliant walls after t_{int} time.

ID	t_{int}	rms displacement
SCW180	$2.74\delta/u_\tau = 495\nu/u_\tau^2$	$30\delta_\nu$
FCW180	$2.74\delta/u_\tau = 495\nu/u_\tau^2$	$501\delta_\nu$
SCW1000	$0.50\delta/u_\tau = 495\nu/u_\tau^2$	$393\delta_\nu$
FCW1000	$0.50\delta/u_\tau = 495\nu/u_\tau^2$	$764\delta_\nu$

4. Conclusions

Active and passive flow control strategies for drag reduction have been investigated by means of direct numerical simulations of canonical channel flows at friction Reynolds numbers of 180 and 1000. The active control technique used herein was proposed by Choi *et al.* [25], and promoted solely streamwise wall fluctuations driven by the streamwise wall shear stress. The passive control technique comprised a compliant surface based on an array of damped harmonic oscillators that ensured solely streamwise wall fluctuations similar to those of the foregoing active control approach. Our previous studies demonstrated [34, 39, 40] that the foregoing conceptual compliant surface can sustain drag reduction by exploiting behaviour similar to that of active control. Using direct numerical simulation, we have uncovered the corresponding drag reduction mechanism.

For detailed analysis, active control techniques were selected, in addition to relatively flexible and stiff compliant surfaces. It has been demonstrated that, when successful, both active and passive control methods reduce spanwise vorticity fluctuations at the wall (and hence the shear between velocity streaks and the wall). By doing so, the control techniques inevitably strengthen shear between the streaks, leading to increased wall-normal vorticity fluctuations. The former effect seems to be beneficial from the drag reduction point of view, whereas the second appears to limit control performance. The Reynolds stress, vorticity, and Reynolds stress transport statistics suggest that reducing spanwise vorticity fluctuations at the wall effectively lower vorticity fluctuations and momentum transfer over the majority of the turbulent boundary layer. The drag reduction mechanisms of the investigated active and passive control methods differ from established flow control strategies, such as opposition control [25–28] and spanwise wall oscillations [37, 59]. According to the Lagrangian displacement field analysis, large-scale wall motions are required to achieve a modest friction drag reduction.

Acknowledgements

The authors are grateful to AkzoNobel's Marine Coatings business (International Paint Ltd) and the Energy Technology Partnership [ETP106] for financial support. We would like to thank the UK Turbulence Consortium and Dr. Sylvain Laizet of Imperial College London for supporting the research with computational resources, and Kirsty Jean Grant for proofreading the manuscript. DNS computations were carried out on the ARCHER UK National Supercomputing Service (http://www.archer.ac.uk).

Appendix A. Baseline velocity and vorticity statistics

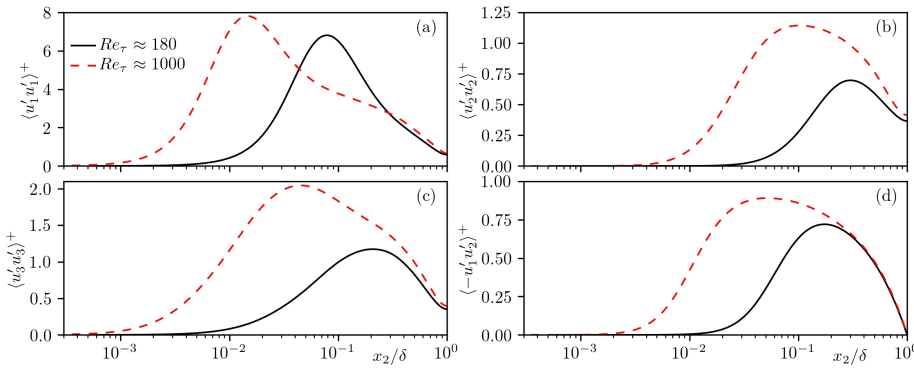

Figure A.8: Reynolds stresses as functions of the wall distance and Reynolds number: streamwise (a), wall-normal (b), spanwise (c) components, and Reynolds shear stress (d).

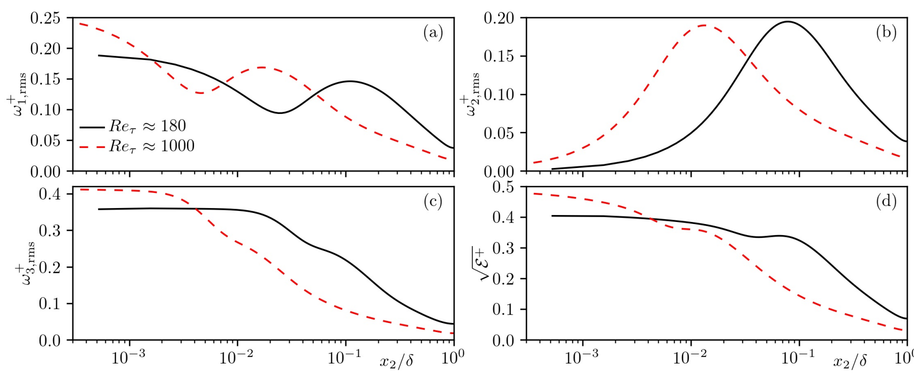

Figure A.9: Vorticity statistics as functions of the wall distance and Reynolds number: streamwise (a), wall-normal (b), spanwise (c) components, and square root of turbulent enstrophy representing the magnitude of the fluctuating vorticity vector (d).

Appendix B. Baseline Reynolds stress transport budgets

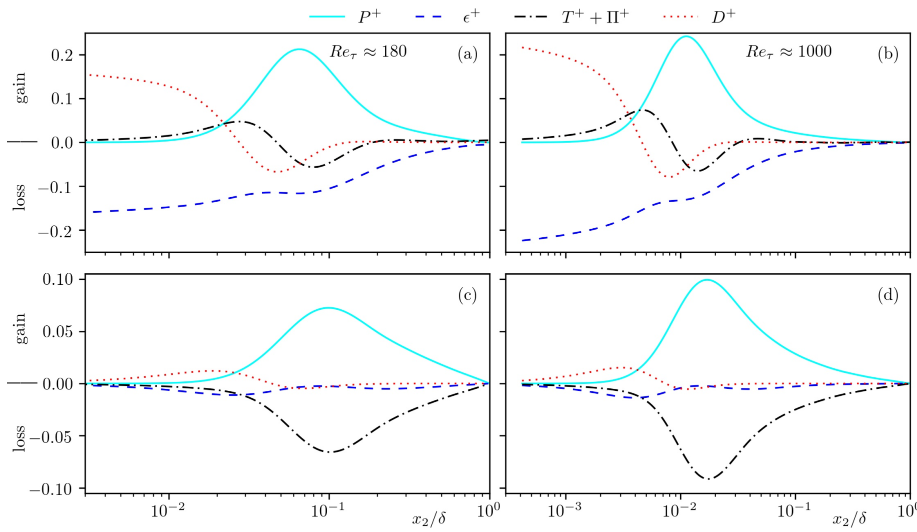

Figure B.10: Turbulent kinetic energy and Reynolds shear stress transport terms as functions of the wall distance at $\mathrm{Re}_\tau \approx 180$ (left column) and at $\mathrm{Re}_\tau \approx 1000$ (right column): turbulent kinetic energy (a)-(b) and Reynolds shear stress $-\langle u_1' u_2' \rangle$ (c)-(d).

References

[1] M. Gad-el-Hak, Compliant coatings for drag reduction, Progress in Aerospace Sciences 38 (1) (2002) 77–99.

[2] M. O. Kramer, Boundary layer stabilization by distributed damping, Journal of Aerosol Science 24 (1957) 459–460.

[3] M. O. Kramer, Boundary layer stabilization by distributed damping, Journal of the American Society for Naval Engineers 72 (1) (1960) 25–34.

[4] M. O. Kramer, Boundary layer stabilization by distributed damping, Naval Engineers Journal 74 (1962) 341–348.

[5] P. W. Carpenter, A. D. Garrad, The hydrodynamic stability of flow over Kramer-type compliant surfaces. Part 1: Tollmien-Schlichting instabilities, Journal of Fluid Mechanics 155 (1985) 465–510.

[6] P. W. Carpenter, A. D. Garrad, The hydrodynamic stability of flow over Kramer-type compliant surfaces. Part 2: Flow-induced surface instabilities, Journal of Fluid Mechanics 170 (1986) 199–232.

[7] C. Davies, P. W. Carpenter, Numerical simulation of the evolution of Tollmien–Schlichting waves over finite compliant panels, Journal of Fluid Mechanics 335 (1997) 361–392.

[8] C. Davies, P. W. Carpenter, Instabilities in a plane channel flow between compliant walls, Journal of Fluid Mechanics 352 (1997) 205–243.

[9] T. Lee, M. Fisher, W. H. Schwarz, Investigation of the stable interaction of a passive compliant surface with a turbulent boundary layer, Journal of Fluid Mechanics 257 (1993) 373.

[10] T. Lee, M. Fisher, W. H. Schwarz, The measurement of flow-induced surface displacement on a compliant surface by optical holographic interferometry, Experiments in Fluids 14 (3) (1993) 159–168.

[11] T. Lee, M. Fisher, W. H. Schwarz, Investigation of the effects of a compliant surface on boundary-layer stability, Journal of Fluid Mechanics 288 (1995) 37–58.

[12] Z. Wang, K. S. Yeo, B. C. Khoo, Spatial direct numerical simulation of transitional boundary layer over compliant surfaces, Computers & Fluids 34 (9) (2005) 1062–1095.

[13] Z. Wang, K. S. Yeo, B. C. Khoo, On two-dimensional linear waves in Blasius boundary layer over viscoelastic layers, European Journal of Mechanics-B/Fluids 25 (1) (2006) 33–58.

[14] J. H. Duncan, J. S. Sirkis, The generation of wave patterns on anisotropic coatings by pressure fluctuations in a turbulent boundary layer, Journal of Sound and Vibration 157 (2) (1992) 243–264.

[15] R. J. Hansen, D. L. Hunston, Fluid-property effects on flow-generated waves on a compliant surface, Journal of Fluid Mechanics 133 (1983) 161–177.

[16] V. M. Kulik, Propagation of deformation waves in a compliant coating, Journal of Engineering Physics and Thermophysics 77 (4) (2004) 753–757.

[17] V. M. Kulik, S. V. Rodyakin, I. Lee, H. H. Chun, Deformation of a viscoelastic coating under the action of convective pressure fluctuations, Experiments in Fluids 38 (5) (2005) 648–655.

[18] S. Xu, D. Rempfer, J. Lumley, Turbulence over a compliant surface: numerical simulation and analysis, Journal of Fluid Mechanics 478 (2003) 11–34.

[19] K. Fukagata, S. Kern, P. Chatelain, P. Koumoutsakos, N. Kasagi, Evolutionary optimization of an anisotropic compliant surface for turbulent friction drag reduction, Journal of Turbulence 9 (2008) 37–41.

[20] E. Kim, H. Choi, Space–time characteristics of a compliant wall in a turbulent channel flow, Journal of Fluid Mechanics 756 (2014) 30–53.

[21] Q.-J. Xia, W.-X. Huang, C.-X. Xu, Direct numerical simulation of turbulent boundary layer over a compliant wall, Journal of Fluids and Structures 71 (2017) 126–142.

[22] M. E. Rosti, L. Brandt, Numerical simulation of turbulent channel flow over a viscous hyper-elastic wall, Journal of Fluid Mechanics 830 (2017) 708–735.

[23] M. Luhar, A. S. Sharma, B. J. McKeon, A framework for studying the effect of compliant surfaces on wall turbulence, Journal of Fluid Mechanics 768 (2015) 415–441.

[24] M. Luhar, A. S. Sharma, B. J. McKeon, On the design of optimal compliant walls for turbulence control, Journal of Turbulence 17 (8) (2016) 787–806.

[25] H. Choi, P. Moin, J. Kim, Active turbulence control for drag reduction in wall-bounded flows, Journal of Fluid Mechanics 262 (1994) 75–110.

[26] T. Endo, N. Kasagi, Y. Suzuki, Feedback control of wall turbulence with wall deformation, International Journal of Heat and Fluid Flow 21 (5) (2000) 568–575.

[27] M. Pamiès, E. Garnier, A. Merlen, P. Sagaut, Opposition control with arrayed actuators in the near-wall region of a spatially developing turbulent boundary layer, International Journal of Heat and Fluid Flow 32 (3) (2011) 621–630.

[28] A. Stroh, B. Frohnapfel, P. Schlatter, Y. Hasegawa, A comparison of opposition control in turbulent boundary layer and turbulent channel flow, Physics of Fluids 27 (7) (2015) 075101.

[29] R. Nakanishi, H. Mamori, K. Fukagata, Relaminarization of turbulent channel flow using

traveling wave-like wall deformation, International Journal of Heat and Fluid Flow 35 (2012) 152–159.

[30] C. Zhang, R. Miorini, J. Katz, Integrating Mach-Zehnder interferometry with TPIV to measure the time-resolved deformation of a compliant wall along with the 3D velocity field in a turbulent channel flow, Experiments in Fluids 56 (11) (2015) 203.

[31] C. Zhang, J. Wang, W. Blake, J. Katz, Deformation of a compliant wall in a turbulent channel flow, Journal of Fluid Mechanics 823.

[32] H. O. G. Benschop, A. J. Greidanus, R. Delfos, J. Westerweel, W.-P. Breugem, Deformation of a linear viscoelastic compliant coating in a turbulent flow, Journal of Fluid Mechanics 859 (2019) 613–658.

[33] T. Endo, R. Himeno, Direct numerical simulation of turbulent flow over a compliant surface, Journal of Turbulence 3.

[34] T. I. Józsa, E. Balaras, M. Kashtalyan, A. G. L. Borthwick, I. M. Viola, Active and passive in-plane wall fluctuations in turbulent channel flows, Journal of Fluid Mechanics 866 (2019) 689–720.

[35] H. O. G. Benschop, W.-P. Breugem, Oscillatory laminar shear flow over a compliant viscoelastic layer on a rigid base, available at https://arxiv.org/pdf/1705.04479.pdf, Accessed 17/03/2020.

[36] P. T. Nagy, G. Paál, Stabilization of the boundary layer by streamwise control, Physics of Fluids 31 (12) (2019) 124107.

[37] L. Agostini, E. Touber, M. A. Leschziner, Spanwise oscillatory wall motion in channel flow: drag-reduction mechanisms inferred from DNS-predicted phase-wise property variations at $\mathrm{Re}_\tau = 1000$, Journal of Fluid Mechanics 743 (2014) 606–635.

[38] T. Min, J. Kim, Effects of hydrophobic surface on skin-friction drag, Physics of Fluids 16 (7) (2004) L55–L58.

[39] T. I. Józsa, Drag Reduction by Passive In-Plane Wall Motions in Turbulent Wall-Bounded Flows, Ph.D. thesis, University of Edinburgh (2018).

[40] T. I. Józsa, E. Balaras, M. Kashtalyan, A. G. L. Borthwick, I. M. Viola, On active and passive streamwise wall fluctuations in turbulent channel flows: a DNS study, 11^{th} International Symposium on Turbulence and Shear Flow Phenomena (TSFP11), Southampton, UK, 30/07/2019–02/08/2019.

[41] S. B. Pope, Turbulent Flows, Cambridge University Press, 2000.

[42] J. Van Kan, A second-order accurate pressure-correction scheme for viscous incompressible flow, SIAM Journal on Scientific and Statistical Computing 7 (3) (1986) 870–891.

[43] P. N. Swarztrauber, A direct method for the discrete solution of separable elliptic equations, SIAM Journal on Numerical Analysis 11 (6) (1974) 1136–1150.

[44] W. H. Press, Numerical recipes 3^{rd} edition: The art of scientific computing, Cambridge University Press, 2007.

[45] E. Balaras, Modeling complex boundaries using an external force field on fixed Cartesian grids in large-eddy simulations, Computers & Fluids 33 (3) (2004) 375–404.

[46] D. J. Wise, P. Ricco, Turbulent drag reduction through oscillating discs, Journal of Fluid Mechanics 746 (2014) 536–564.

[47] P. Ricco, C. Ottonelli, Y. Hasegawa, M. Quadrio, Changes in turbulent dissipation in a channel flow with oscillating walls, Journal of Fluid Mechanics 700 (2012) 77–104.

[48] M. J. Walsh, Riblets as a viscous drag reduction technique, AIAA journal 21 (4) (1983) 485–486.

[49] H. Choi, P. Moin, J. Kim, Direct numerical simulation of turbulent flow over riblets, Journal of Fluid Mechanics 255 (1993) 503–539.

[50] R. García-Mayoral, J. Jiménez, Drag reduction by riblets, Philosophical transactions of

the Royal society A: Mathematical, physical and engineering Sciences 369 (1940) (2011) 1412–1427.

[51] S. Ghebali, S. I. Chernyshenko, M. A. Leschziner, Can large-scale oblique undulations on a solid wall reduce the turbulent drag?, Physics of Fluids 29 (10) (2017) 105102.

[52] J. Jiménez, A. Pinelli, The autonomous cycle of near-wall turbulence, Journal of Fluid Mechanics 389 (1999) 335–359.

[53] R. J. Adrian, Hairpin vortex organization in wall turbulence, Physics of Fluids 19 (4) (2007) 041301.

[54] J. Jiménez, Near-wall turbulence, Physics of Fluids 25 (10) (2013) 101302.

[55] L. Agostini, E. Touber, M. A. Leschziner, The turbulence vorticity as a window to the physics of friction-drag reduction by oscillatory wall motion, International Journal of Heat and Fluid Flow 51 (2015) 3–15.

[56] J. C. R. Hunt, A. A. Wray, P. Moin, Eddies, streams, and convergence zones in turbulent flows, Tech. rep., NASA (1988).

[57] P. Moin, J. Kim, The structure of the vorticity field in turbulent channel flow. Part 1. Analysis of instantaneous fields and statistical correlations, Journal of Fluid Mechanics 155 (1985) 441–464.

[58] J. Kim, P. Moin, The structure of the vorticity field in turbulent channel flow. Part 2. Study of ensemble-averaged fields, Journal of Fluid Mechanics 162 (1986) 339–363.

[59] M. Quadrio, P. Ricco, Critical assessment of turbulent drag reduction through spanwise wall oscillations, Journal of Fluid Mechanics 521 (2004) 251–271.

[60] T. I. Józsa, Analytical solutions of incompressible laminar channel and pipe flows driven by in-plane wall oscillations, Physics of Fluids 31 (8) (2019) 083605.

[61] B. J. Balakumar, R. J. Adrian, Large-and very-large-scale motions in channel and boundary-layer flows, Philosophical Transactions of the Royal Society of London A: Mathematical, Physical and Engineering Sciences 365 (1852) (2007) 665–681.

[62] R. Mathis, N. Hutchins, I. Marusic, Large-scale amplitude modulation of the small-scale structures in turbulent boundary layers, Journal of Fluid Mechanics 628 (2009) 311–337.

[63] N. N. Mansour, J. Kim, P. Moin, Reynolds-stress and dissipation-rate budgets in a turbulent channel flow, Journal of Fluid Mechanics 194 (1988) 15–44.

[64] K. Fukagata, K. Iwamoto, N. Kasagi, Contribution of Reynolds stress distribution to the skin friction in wall-bounded flows, Physics of Fluids 14 (11) (2002) L73–L76.

[65] M. Yoon, J. Ahn, J. Hwang, H. J. Sung, Contribution of velocity-vorticity correlations to the frictional drag in wall-bounded turbulent flows, Physics of Fluids 28 (8) (2016) 081702.